


Modulation of the probe signal in coherent phonon detection revisited: Analytical and first-principles computational analyses

Atsushi Yamada * and Kazuhiro Yabana

Center for Computational Sciences, University of Tsukuba, 1-1-1 Tennodai, Tsukuba, Ibaraki 305-8577, Japan



(Received 21 April 2020; revised manuscript received 15 June 2020; accepted 16 June 2020; published 29 June 2020)

Modulation of probe signals in pump-probe measurements of coherent phonons in dielectrics, with and without spectral resolution, are investigated theoretically taking diamond as an example. Analytical investigation as well as first-principles calculations based on time-dependent density-functional theory is utilized to clarify the mechanism of the modulation of the probe signals. Boundary and bulk effects are investigated systematically, putting emphasis on the phase relation between the modulation and the atomic motion of the coherent phonon. They are summarized as follows: Modulation by the boundary effect is in phase with the coherent phonon amplitude, while that by the bulk effect shows $\pi/2$ phase difference. Strong frequency dependence appears in the modulation by the bulk effect, while no frequency dependence by the boundary effect. First-principles calculations support the reliability of the analytical result.

DOI: [10.1103/PhysRevB.101.214313](https://doi.org/10.1103/PhysRevB.101.214313)

I. INTRODUCTION

Coherent phonon generation is commonly observed when an intense and ultrashort light pulse irradiates on the surface of a bulk material. It is usually measured using a pump-probe method in the following way. A strong pump pulse generates the vibrational motion of atoms in the medium that has a coherence in space and time. A weak probe pulse is then used to detect the coherent phonon through a measurement of the modulation of the optical response induced by the atomic displacements. Mechanisms for the generation of coherent phonons in simple crystalline solids have been extensively discussed since the middle of the '80s in both theoretical and experimental perspectives [1–24].

Recent research has been extended to further manipulations by, for example, using multipump pulses to control the phonon amplitude [11,13,25], using stronger pulses to give rise to a large amplitude oscillation that may possibly realize a photoinduced phase transition [26–33]. Investigations have also been extended to systems other than bulk materials such as graphene and two-dimensional materials [34–36], and solids composed of biological molecules [37].

In this paper, we devote ourselves to theoretical investigations of the probe stage of pump-probe measurements of coherent phonons in transparent materials. For the generation of coherent phonons in transparent materials, an impulsive stimulated Raman scattering (ISRS) mechanism has been widely accepted [5,13,17]. In this mechanism, the pump pulse brings virtual electronic excitations in the medium during the irradiation that causes the impulsive force acting on atoms. In the probe stage, modulations of the reflectivity or the transmittivity are usually measured and analyzed using a simple and

intuitive formula [5],

$$\frac{\Delta R}{R} \propto \frac{\partial R}{\partial n} \frac{\partial n}{\partial Q} Q(t), \quad (1)$$

where n is the index of refraction and Q is the phonon amplitude. It can be derived assuming that the modulation takes place at the surface of the medium. Using this formula, the modulation is proportional to the phonon amplitude. Below, we call this mechanism of the modulation the boundary effect. In the probe state, the significance of the bulk effect has also been discussed immediately after the observation of the coherent phonon generation by the ISRS mechanism [2,3]. It has been pointed out that it shows a phase shift of $\pi/2$ with respect to the phonon oscillation, that is, the modulation is maximum when the phonon amplitude is zero [2,3,5,38]. However, the bulk effect has not been observed much since the effect is suppressed by phase mismatch in practical systems [5,38].

In measurements of modulations of the probe signal, spectrally resolved signals have also been reported [5,9,10,16]. In these measurements, it has been reported that the measured spectra show a phase difference of π between Stokes and anti-Stokes frequency components that correspond to above and below the central frequency of the probe pulse, respectively. In Ref. [5], it was clearly discussed that the phase difference can be explained as the bulk effect mentioned above. In the works afterward [9,10,16], however, the bulk effect was not discussed. In Ref. [10], instead, it has been argued that the quadratic dispersion of the Raman tensor is responsible for the modulation. At present, we consider that it is important to organize the effects that appear in the probe stage of coherent phonon measurements, the boundary and the bulk effects, and signals with and without spectral resolution.

In this paper, we will investigate the modulation of the probe signal employing two approaches. We first discuss an analytic treatment that has been developed previously [5,38].

*ayamada@ccs.tsukuba.ac.jp

Starting with a propagation equation that describes the probe process of the coherent phonon, an approximate analytic solution is constructed. Using the solution, analytic formulas for the modulation of the reflection and transmission rates are constructed, separating the boundary and the bulk effects, with and without spectral resolution. We next present a first-principles computational approach based on time-dependent density-functional theory (TDDFT) [39,40]. Based on the TDDFT, a formalism and computational methods to calculate electron dynamics in real time have been developed [41,42]. For the coherent phonon generation, it was shown that the TDDFT is capable of describing two generation mechanisms of coherent phonons, ISRS and dispersive excitation mechanisms [43,44]. Recently, it has been further extended to describe ionic motion as well as electromagnetic fields simultaneously. There are two approaches to realize it: One is the multiscale approach where the coupled dynamics of macroscopic electromagnetic fields and microscopic dynamics of electrons and ions are described [45,46]. The other is the microscopic approach where the coupled dynamics are described at the same scale [47,48]. In our analysis, we utilize the former multiscale approach.

The organization of the present paper is as follows. In Sec. II, an analytic approach for the modulation of the probe process of coherent phonon is developed. In Sec. III, the first-principles computational approach is explained. In Sec. IV, results by the first-principles calculations and by the analytical theory are compared. Discussions on previous publications are also given. A summary is presented in Sec. V.

II. ANALYTICAL CONSIDERATION

A. Setup of the system

We consider a pump-probe measurement of coherent phonon generation in diamond and focus on the probe stage. We set the coordinate system such that the [100] direction of the cubic diamond crystal structure coincides with the x axis. The surface of the diamond locates at the $x = 0$ plane, a medium in $x > 0$, and a vacuum in $x < 0$ regions. We set the [010] direction parallel to the y axis, and [001] to the z axis.

The coherent phonon is assumed to be generated by a pump pulse in the ISRS mechanism as described below. The pump pulse is linearly polarized in the [011] direction and propagates along the [100] direction. The duration of the pulse is much shorter than the period of the optical phonon and the average frequency is much below the band gap of the diamond. The pump pulse reaches the surface of the diamond at $t = 0$, and propagates with the group velocity of $v_g = c/n_g$, where n_g is the group index of refraction of the diamond. In the following development, we ignore frequency dependence of the susceptibility. Therefore, we use the index of refraction n instead of n_g below. The atomic displacements of the coherent phonon are along the [100] direction.

We express the atomic displacement at the position x as

$$\Delta \mathbf{R}^{\pm} \propto \pm(Q(x, t), 0, 0), \quad (2)$$

where the sign \pm indicates that there are two possible directions of the atomic displacements in the optical phonon. The

phonon displacement $Q(x, t)$ is given by

$$Q(x, t) = \theta(x)q\left(t - \frac{n}{c}x\right), \quad (3)$$

where the step function $\theta(x)$ is introduced to indicate the spatial region of the medium. The function $q(t)$ describes the phonon amplitude at the surface $x = 0$. We assume a sinusoidal form,

$$q(t) = q_0 \sin(\Omega t), \quad (4)$$

with the phonon amplitude q_0 and the frequency of the optical phonon Ω . We ignore the damping of the coherent phonon for simplicity.

The coherent phonon induces anisotropy in the refractive index of the diamond in which the optical axes are given by the [011] and [01 $\bar{1}$] directions. The anisotropy is measured in time domain using the probe pulse whose duration is much shorter than the period of the phonon. As the probe process, we consider the electro-optic (EO) sampling method that has often been used to detect the signal of the coherent phonon [4,7,19]. In the method, the probe pulse is linearly polarized along the [010] direction that is 45° to the polarization direction of the pump pulse ([011] direction). The Raman scattering wave polarized in the [001] direction is then induced by the interaction between the incident probe pulse and the coherent phonon. The probe signal is then decomposed into the parallel ([011]) and the perpendicular ([01 $\bar{1}$]) components with respect to the direction of the pump polarization. The difference in the modulations that are recorded in the two components provides the information on the coherent phonon.

We investigate the modulation of the probe signal, classifying into four cases for reflection and transmission signals with and without spectral resolution. For the reflected and the transmitted probe pulses, we introduce the frequency-resolved fluences, $F_{\parallel, \perp}^{(r)}(\omega; \delta)$, and $F_{\parallel, \perp}^{(t)}(\omega; \delta)$, respectively, where \parallel, \perp indicate parallel and perpendicular components, ω is the frequency of the probe pulse, and δ specifies the delay time between the pump and the probe pulses. The reflected and transmitted intensities in the absence of the coherent phonon are denoted as $F_0^{(r)}(\omega)$ and $F_0^{(t)}(\omega)$, respectively. The subscript 0 is used also for other quantities to denote the absence of the coherent phonon.

The spectrally resolved modulation of the reflectance is defined by

$$\frac{\Delta R_{\parallel, \perp}(\omega; \delta)}{R_0(\omega)} = \frac{\Delta F_{\parallel, \perp}^{(r)}(\omega; \delta)}{F_0^{(r)}(\omega)}, \quad (5)$$

where $\Delta R_{\parallel, \perp}$ and $\Delta F_{\parallel, \perp}$ indicate the difference from those without the coherent phonon, that is, $\Delta R_{\parallel, \perp} = R_{\parallel, \perp} - R_0$ and $\Delta F_{\parallel, \perp}^{(r)} = F_{\parallel, \perp}^{(r)} - F_0^{(r)}$. We also introduce a modulation without spectral resolution:

$$\frac{\Delta R_{\parallel, \perp}(\delta)}{R_0} = \frac{\int d\omega F_{\parallel, \perp}^{(r)}(\omega; \delta)}{\int d\omega F_0^{(r)}(\omega)}. \quad (6)$$

The signal of the EO sampling is then given by

$$\Delta R_{\text{EO}}(\delta)/R_0 = (\Delta R_{\perp}(\delta) - \Delta R_{\parallel}(\delta))/R_0. \quad (7)$$

We introduce similar quantities for the transmission.

B. Propagation equation

To describe the modulation of the probe pulse, we start from the one-dimensional equation for light propagation,

$$\left(\frac{\partial^2}{\partial x^2} - \frac{1}{c^2} \frac{\partial^2}{\partial t^2}\right) \mathbf{E}(x, t) = \theta(x) \frac{4\pi}{c^2} \frac{\partial^2 \mathbf{P}(x, t)}{\partial t^2}, \quad (8)$$

where $\mathbf{E}(x, t)$ and $\mathbf{P}(x, t)$ are the electric field of the probe pulse and the induced polarization at position x and at time t . The step function $\theta(x)$ indicates that the medium is in the $x > 0$ region. For the polarization, we assume a linear and instantaneous relation to the electric field as follows:

$$\begin{pmatrix} P_x \\ P_y \\ P_z \end{pmatrix} = \chi \begin{pmatrix} E_x \\ E_y \\ E_z \end{pmatrix} + \frac{\partial \chi_{yz}}{\partial Q} Q \begin{pmatrix} 0 & 0 & 0 \\ 0 & 0 & 1 \\ 0 & 1 & 0 \end{pmatrix} \begin{pmatrix} E_x \\ E_y \\ E_z \end{pmatrix}, \quad (9)$$

where χ is the linear isotropic susceptibility at the equilibrium atomic configuration, and $\partial \chi_{yz}/\partial Q$ is the coefficient of the Raman tensor. We denote $\partial \chi_{yz}/\partial Q$ as χ_R below to simplify the formula. We ignore any retardation effects in the analyses in the following development. It is equivalent to ignoring the frequency dependence of χ and χ_R in the frequency representation.

Equation (8) can be decoupled by introducing parallel and perpendicular components of the electric field,

$$E_{\parallel, \perp} = \frac{1}{\sqrt{2}} (E_y \pm E_z). \quad (10)$$

The propagation equations for the E_{\parallel} and E_{\perp} are given by

$$\frac{\partial^2}{\partial x^2} E_{\parallel, \perp} - \frac{n(x)^2}{c^2} \frac{\partial^2}{\partial t^2} E_{\parallel, \perp} = \pm \frac{4\pi \chi_R}{c^2} \frac{\partial^2}{\partial t^2} [QE_{\parallel, \perp}], \quad (11)$$

$$\delta E_{\parallel, \perp}(x, t) = \begin{cases} \mp \frac{4\pi \chi_R}{n(n+1)^2} q(t + \frac{x}{c}) e^{(i)}(t + \frac{x}{c} - \delta) & (x < 0) \\ \mp \frac{4\pi \chi_R}{n(n+1)^2} \left\{ 1 + \frac{(n+1)x}{c} \frac{d}{dt} \right\} q(t - \frac{nx}{c}) e^{(i)}(t - \frac{nx}{c} - \delta) & (x > 0). \end{cases} \quad (16)$$

We note that the transmitted wave includes the stimulated Raman wave whose amplitude increases linearly with the propagation distance x .

C. Modulation effects

We evaluate the modulation of the reflectivity in the vacuum region, $x < 0$, and the modulation of the transmittivity in the medium region, $x > 0$. To evaluate the fluence of the pulse, we utilize the Poynting vector $S(x, t)$ that is given in terms of the electric and the magnetic fields by

$$S(x, t) = \frac{c}{4\pi} E(x, t) H(x, t). \quad (17)$$

The fluence of the pulsed light is given as the time integration of the Poynting vector:

$$F(x) = \int dt S(x, t). \quad (18)$$

To analyze the frequency component of the fluence, we introduce the spectral decomposition of the fluence as

$$F(x) = \int_0^\infty d\omega F(x, \omega), \quad (19)$$

$$F(x, \omega) = \frac{c}{4\pi^2} \text{Re}[E(x, \omega) H^*(x, \omega)], \quad (20)$$

where the positive sign (+) is for E_{\parallel} and the negative sign (−) for E_{\perp} on the right-hand side. The index of refraction $n(x)$ is given by

$$n(x) = \begin{cases} 1 & (x < 0) \\ n & (x > 0), \end{cases} \quad (12)$$

where n is given by $n = \sqrt{1 + 4\pi \chi}$.

In the following, we treat the modulation of the susceptibility caused by the coherent phonon, the right-hand side of Eq. (11), as a perturbation. First we construct the unperturbed solution, ignoring the right-hand side of Eq. (11). We express the time profile of the incident electric field as $e^{(i)}(t)$, which is a pulsed field centered at $t = 0$. The unperturbed solution which we denote as $E_0(x, t)$ is given as follows:

$$E_0(x, t) = \begin{cases} e^{(i)}(t - \delta - \frac{x}{c}) - \frac{n-1}{n+1} e^{(i)}(t - \delta + \frac{x}{c}), & (x < 0) \\ \frac{2}{n+1} e^{(i)}(t - \delta - \frac{nx}{c}). & (x > 0), \end{cases} \quad (13)$$

where the center of the incident pulse, $e^{(i)}(t - \delta - x/c)$, is set to arrive at the surface $x = 0$ at time $t = \delta$.

We denote the electric field including the perturbed field generated by the coherent phonon as

$$E_{\parallel, \perp}(x, t) = E_0(x, t) + \delta E_{\parallel, \perp}(x, t). \quad (14)$$

The perturbed fields, $\delta E_{\parallel, \perp}(x, t)$, satisfy

$$\frac{\partial^2}{\partial x^2} \delta E_{\parallel, \perp} - \frac{n(x)^2}{c^2} \frac{\partial^2}{\partial t^2} \delta E_{\parallel, \perp} = \pm \frac{4\pi \chi_R}{c^2} \frac{\partial^2}{\partial t^2} [QE_0]. \quad (15)$$

As is easily verified, the solution of this equation is given by

where $E(x, \omega)$ and $H(x, \omega)$ are the Fourier transforms of $E(x, t)$ and $H(x, t)$, respectively.

We first consider the reflectivity and transmittivity in the absence of the coherent phonon and confirm that we obtain well-known results. The fluences for the incident, reflected, and transmitted waves that are resolved in frequency, $F_0^{(i)}(\omega)$, $F_0^{(r)}(\omega)$, $F_0^{(t)}(\omega)$, respectively, are given by

$$F_0^{(i)}(\omega) = \frac{c}{4\pi^2} |e^{(i)}(\omega)|^2, \quad (21)$$

$$F_0^{(r)}(\omega) = \frac{c}{4\pi^2} \left(\frac{n-1}{n+1} \right)^2 |e^{(i)}(\omega)|^2, \quad (22)$$

$$F_0^{(t)}(\omega) = \frac{c}{4\pi^2} \frac{4n}{(n+1)^2} |e^{(i)}(\omega)|^2, \quad (23)$$

where $e^{(i)}(\omega)$ is the Fourier transformation of the incident pulse $e^{(i)}(t)$. The sign of $F_0^{(r)}$ is defined as positive for the backward direction from the material region. The frequency-resolved reflectivity and transmittivity are obtained as

$$R_0(\omega) = \frac{F_0^{(r)}(\omega)}{F_0^{(i)}(\omega)} = \left(\frac{n-1}{n+1} \right)^2, \quad (24)$$

$$T_0(\omega) = \frac{F_0^{(t)}(\omega)}{F_0^{(i)}(\omega)} = \frac{4n}{(n+1)^2}. \quad (25)$$

We note that the reflectivity and transmittivity show no frequency dependence if we ignore the frequency dependence in the index of refraction.

We next move to the perturbative contributions generated by the coherent phonon. We calculate them by Eq. (20) using the electric field of Eq. (16) and corresponding magnetic field. The modulation in the fluence of reflected wave is calculated as

$$\delta F_{\parallel,\perp}^{(r)}(\omega) = \pm \frac{c\chi_R(n-1)q_0}{\pi n(n+1)^3} \text{Im}W(\omega, \delta), \quad (26)$$

where $W(\omega, \delta)$ is introduced by

$$W(\omega, \delta) = e^{(i)*}(\omega) \{ e^{i\Omega\delta} e^{(i)}(\omega + \Omega) - e^{-i\Omega\delta} e^{(i)}(\omega - \Omega) \}. \quad (27)$$

From this result, the modulation of the frequency-resolved reflectivity is calculated as

$$\frac{\Delta R_{\parallel,\perp}(\omega, \delta)}{R_0(\omega)} = \pm \frac{4\pi\chi_R q_0}{n(n^2-1)} \frac{\text{Im}W(\omega, \delta)}{|e^{(i)}(\omega)|^2}. \quad (28)$$

The modulation of the reflectivity without the frequency resolution is given by

$$\frac{\Delta R_{\parallel,\perp}(\delta)}{R_0} = \pm \frac{8\pi\chi_R}{n(n^2-1)} \frac{\int q(t+\delta)(e^{(i)}(t))^2 dt}{\int (e^{(i)}(t))^2 dt}. \quad (29)$$

Assuming that the probe pulse is much shorter than the period of the coherent phonon, $2\pi/\Omega$, the equation is approximated to a simpler form:

$$\frac{\Delta R_{\parallel,\perp}(\delta)}{R_0} \simeq \pm \frac{8\pi\chi_R q_0}{n(n^2-1)} \sin(\Omega\delta). \quad (30)$$

We note that the modulation is in phase with the phonon amplitude and that this expression coincides with an intuitive expression of Eq. (1), assuming the instantaneous modulation of the susceptibility given by $\chi(t) = \chi + \chi_R q(t)$ at the surface:

$$\frac{\Delta R_{\parallel,\perp}(\delta)}{R_0} = \frac{1}{R_0} \frac{\partial R}{\partial n_{\parallel,\perp}} \frac{\partial n_{\parallel,\perp}}{\partial Q} q_0 \sin(\Omega\delta). \quad (31)$$

The signals of the EO sampling defined by Eq. (7) are then written by

$$\frac{\Delta R_{\text{EO}}(\omega, \delta)}{R_0(\omega)} = - \frac{8\pi\chi_R q_0}{n(n^2-1)} \frac{\text{Im}W(\omega, \delta)}{|e^{(i)}(\omega)|^2}, \quad (32)$$

$$\frac{\Delta R_{\text{EO}}(\delta)}{R_0} = - \frac{16\pi\chi_R}{n(n^2-1)} \frac{\int q(t+\delta)(e^{(i)}(t))^2 dt}{\int (e^{(i)}(t))^2 dt}, \quad (33)$$

$$\sim - \frac{16\pi\chi_R q_0}{n(n^2-1)} \sin(\Omega\delta). \quad (34)$$

For the transmittivity, there appear two terms in the modulation of the fluence at $x = l (> 0)$,

$$\begin{aligned} \delta F_{\parallel,\perp}^{(t)}(\omega) &= \mp \frac{c\chi_R}{\pi n(n+1)^3} q_0 \text{Im} \\ &\quad \pm \frac{2\chi_R \omega l}{\pi(n+1)^2} q_0 \text{Re}W(\omega, \delta) [nW(\omega, \delta) + W^*(\omega, \delta)]. \end{aligned} \quad (35)$$

The first term is generated at the surface $x = 0$ and the second term originates from the stimulated Raman wave which is proportional to the propagation length, l . We call the former

the boundary contribution and the latter the bulk contribution. The modulation with the frequency resolution is given by

$$\begin{aligned} \frac{\Delta T_{\parallel,\perp}(\omega, \delta)}{T_0(\omega)} &= \mp \frac{\pi\chi_R q_0}{n^2(n+1)} \frac{\text{Im}[nW(\omega, \delta) + W^*(\omega, \delta)]}{|e^{(i)}(\omega)|^2} \\ &\quad \pm \frac{2\pi\chi_R \omega l q_0}{cn} \frac{\text{Re}W(\omega, \delta)}{|e^{(i)}(\omega)|^2}. \end{aligned} \quad (36)$$

Using Eq. (19), the modulation without the frequency resolution is given by

$$\begin{aligned} \frac{\Delta T_{\parallel,\perp}(\delta)}{T_0} &= \mp \frac{2\pi\chi_R(n-1)}{n^2(n+1)} \frac{\int q(t+\delta)(e^{(i)}(t))^2 dt}{\int (e^{(i)}(t))^2 dt} \\ &\quad \mp \frac{2\pi\chi_R l}{cn} \frac{\int \frac{dq}{dt}(t+\delta)(e^{(i)}(t))^2 dt}{\int (e^{(i)}(t))^2 dt}, \end{aligned} \quad (37)$$

and a simpler expression is obtained by using the short pulse limit approximation as

$$\frac{\Delta T_{\parallel,\perp}(\delta)}{T_0} \simeq \mp \frac{2\pi\chi_R(n-1)q_0}{n^2(n+1)} \sin(\Omega\delta) \mp \frac{2\pi\chi_R l q_0}{cn} \cos(\Omega\delta). \quad (38)$$

From Eqs. (37) and (38), the first sine function terms that originate from the surface come from the phonon amplitude $q(t+\delta)$. It causes in-phase modulation on the time delay as that in the reflection. The second cosine function terms that originate from the stimulated Raman wave are due to the phonon velocity $\frac{dq}{dt}(t+\delta)$ which induces the $\pi/2$ phase-shifted modulation. This expression of the first term again coincides with an intuitive expression of Eq. (1), assuming the instantaneous modulation of the susceptibility $\chi(t) = \chi + \chi_R q(t)$ at the surface,

$$\frac{\Delta T_{\parallel,\perp}^B(\delta)}{T_0} = \frac{1}{T_0} \frac{\partial T}{\partial n_{\parallel,\perp}} \frac{\partial n_{\parallel,\perp}}{\partial Q} q_0 \sin(\Omega\delta), \quad (39)$$

where the superscript B indicates that this originates from the boundary effect.

From Eqs. (36)–(38), the transmission change in the EO sampling is written by

$$\begin{aligned} \frac{\Delta T_{\text{EO}}(\omega, \delta)}{T_0(\omega)} &= - \frac{4\pi\chi_R \omega l q_0}{cn} \frac{\text{Re}W(\omega, \delta)}{|e^{(i)}(\omega)|^2} \\ &\quad + \frac{2\pi\chi_R q_0}{n^2(n+1)} \frac{\text{Im}[nW(\omega, \delta) + W^*(\omega, \delta)]}{|e^{(i)}(\omega)|^2}, \end{aligned} \quad (40)$$

$$\begin{aligned} \frac{\Delta T_{\text{EO}}(\delta)}{T_0} &= \frac{4\pi\chi_R(n-1)}{n^2(n+1)} \frac{\int q(t+\delta)(e^{(i)}(t))^2 dt}{\int (e^{(i)}(t))^2 dt} \\ &\quad + \frac{4\pi\chi_R l}{cn} \frac{\int \frac{dq}{dt}(t+\delta)(e^{(i)}(t))^2 dt}{\int (e^{(i)}(t))^2 dt}, \end{aligned} \quad (41)$$

$$\begin{aligned} &\simeq \frac{4\pi\chi_R(n-1)q_0}{n^2(n+1)} \sin(\Omega\delta) \\ &\quad + \frac{4\pi\chi_R l q_0}{cn} \cos(\Omega\delta). \end{aligned} \quad (42)$$

To simplify the result for the frequency-resolved modulation, we introduce an assumption that $e^{(i)}(\omega)$ is a real-valued function except for a multiplicative complex number.

For example, for a symmetric function, $e^{(i)}(t) = e^{(i)}(-t)$, we have real-valued $e^{(i)}(\omega)$. For an antisymmetric function, $e^{(i)}(t) = -e^{(i)}(-t)$, $e^{(i)}(\omega)$ is a pure imaginary function. Under the assumption and expressing $e^{(i)}(\omega)$, removing the complex phase, we have

$$W(\omega, \delta) = \cos(\Omega\delta)e^{(i)}(\omega)\{e^{(i)}(\omega + \Omega) - e^{(i)}(\omega - \Omega)\} + i \sin(\Omega\delta)e^{(i)}(\omega)\{e^{(i)}(\omega + \Omega) + e^{(i)}(\omega - \Omega)\}. \quad (43)$$

We may further introduce an expansion with respect to Ω that is justified when the probe pulse is much shorter than the period of the coherent phonon. Then $W(\omega, \delta)$ is approximated as

$$W(\omega, \delta) \simeq \cos(\Omega\delta)\Omega \frac{d}{d\omega}(e^{(i)}(\omega))^2 + i \sin(\Omega\delta)(e^{(i)}(\omega))^2. \quad (44)$$

Using this approximation, we get the following simplified expressions for the spectrally resolved modulations:

$$\frac{\Delta R_{\text{EO}}(\omega, \delta)}{R_0(\omega)} \simeq -\frac{8\pi \chi_R q_0}{n(n^2 - 1)} \sin \Omega\delta, \quad (45)$$

$$\frac{\Delta T_{\text{EO}}(\omega, \delta)}{T_0(\omega)} \simeq -\frac{4\pi \chi_R \omega \Omega l q_0}{cn} \cos \Omega\delta \frac{d}{d\omega}(e^{(i)}(\omega))^2 (e^{(i)}(\omega))^2 + \frac{2\pi \chi_R (n-1)q_0}{n^2(n+1)} \sin \Omega\delta. \quad (46)$$

We note that the terms originating from the boundary, the modulation of the reflection, and the second term of the modulation of the transmission, are independent of the frequency in the first-order approximation, while the term originating from the stimulated Raman wave causes the frequency-dependent modulation.

We here mention the relation of our results with previous works. The bulk effect as well as the boundary effect was discussed by Merlin *et al.* [5,38]. Corresponding expressions to Eqs. (28) and (36) were presented there. In particular, the appearance of the frequency dependence as well as the phase change between the bulk and the boundary effects have been stressed. In the present derivation, we provide a unified and detailed explanation of the formula with a precise expression for the amplitude of the modulation, which was not presented in Ref. [5]. In Ref. [10], it was argued that the frequency-dependent modulation cannot be described without introducing a frequency dependence in the Raman tensor. This conclusion contradicts with the present result: The frequency-dependent modulation can be explained if we include the bulk effect.

III. FIRST-PRINCIPLES SIMULATION BASED ON TIME-DEPENDENT DENSITY-FUNCTIONAL THEORY

In the previous section, we used several assumptions and approximations to derive the analytical formula. For example, we ignored the frequency dependence of the Raman tensor as well as the dielectric function. We also take a lowest-order perturbation theory. Harmonic motion is assumed for the phonon motion. In this section, we present a complimentary computational approach based on first-principles TDDFT. We

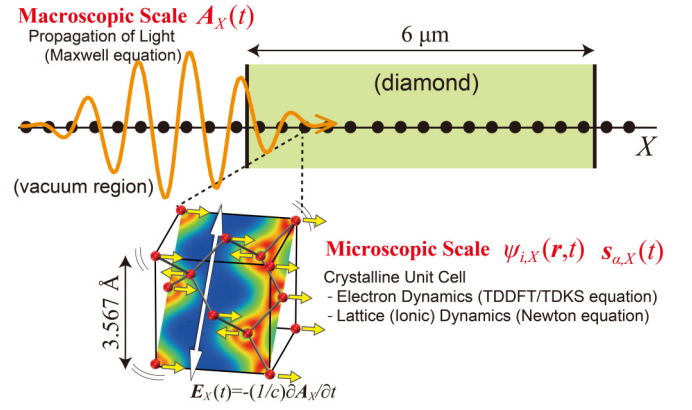


FIG. 1. Schematic illustration of the multiscale model.

develop a multiscale formalism [49] that allows a description of the pump-probe measurement of coherent phonons without any empirical parameters related to materials [45]. A formalism and numerical method are written in this section and calculated results will be presented and compared with analytical results in the next section.

A. Multiscale simulation method

Here we briefly explain our multiscale simulation method. A full explanation has been given in our previous publication [45]. Calculations have been carried out using SALMON, an open source software developed in our group [50,51].

Our simulation describes the pump-probe measurement of the coherent phonon generation faithfully mimicking the setup of the problem. We show the scheme of our simulation in Fig. 1. For an incident pulse propagating along the x axis, we utilize two coordinate systems: The light propagation is described using a one-dimensional coordinate X , which we call the macroscopic coordinate. Microscopic three-dimensional coordinates \mathbf{r} are used to describe the dynamics of electrons and ions.

The light electromagnetic field is expressed by using a vector potential $A_X(t)$. It satisfies the Maxwell equation on the macroscopic scale,

$$\left[\frac{1}{c^2} \frac{\partial^2}{\partial t^2} - \frac{\partial^2}{\partial X^2} \right] A_X(t) = \frac{4\pi}{c} J_X(t), \quad (47)$$

where $J_X(t)$ is the electric current density at the point X .

In solving Eq. (47), we discretize the coordinate X using a uniform grid. At each macroscopic grid point X , we consider a microscopic dynamics of electrons and ions. In our multiscale description, each microscopic dynamics is assumed to be regarded as infinitely periodic. Since the wavelength of the pulsed light is much longer than the typical spatial scale of the microscopic dynamics, we assume a dipole approximation where electrons and ions move under a spatially uniform electric field, $E_X(t) = -(1/c)(\partial A_X(t)/\partial t)$. Then we may apply the Bloch theorem in the microscopic dynamics: The electron motion at macroscopic position X is described using Bloch orbitals $u_{nk,X}(\mathbf{r}, t)$ specified by the macroscopic position X , band index n , and the crystalline momentum \mathbf{k} . Ionic motion

is described by the coordinates of ions in the unit cell, $\mathbf{R}_{\alpha,X}(t)$, where the index α distinguishes different ions in the unit cell.

The Bloch orbitals satisfy the TDKS equation,

$$\begin{aligned} i\hbar \frac{\partial}{\partial t} u_{nk,X}(\mathbf{r}, t) &= \left[\frac{1}{2m} \left\{ -i\hbar \nabla_{\mathbf{r}} + \hbar \mathbf{k} + \frac{e}{c} \mathbf{A}_X(t) \right\}^2 - e\phi_X(\mathbf{r}, t) \right. \\ &\quad \left. + \frac{\delta E_{XC}[n_{e,X}]}{\delta n_{e,X}} + \hat{v}_{\text{ion},X}(\mathbf{r}, t) \right] u_{nk,X}(\mathbf{r}, t) \end{aligned} \quad (48)$$

where $n_{e,X}$ is the electron density given by $n_{e,X}(\mathbf{r}, t) = \sum_{n,k} |u_{nk,X}(\mathbf{r}, t)|^2$. $\phi_X(\mathbf{r}, t)$ and $E_{XC}[n_{e,X}]$ are the Hartree potential and the exchange-correlation energy, respectively. $\hat{v}_{\text{ion},X}(\mathbf{r}, t)$ is the electron-ion potential for which we use norm-conserving pseudopotential [52]. The ionic potential $\hat{v}_{\text{ion},X}$ depends on the ionic coordinates $\{\mathbf{R}_{\alpha,X}(t)\}$ as parameters.

To describe the dynamics of ions, we use a so-called Ehrenfest method [40] where the ionic motion is described by the Newtonian equation,

$$M_{\alpha} \frac{d^2 \mathbf{R}_{\alpha,X}}{dt^2} = -\frac{eZ_{\alpha}}{c} \frac{d\mathbf{A}_X}{dt} - \frac{\partial}{\partial \mathbf{R}_{\alpha,X}} \int d\mathbf{r} [en_{\text{ion},X} \phi_X], \quad (49)$$

where M_{α} is the mass of the α th ion, $n_{\text{ion},X}$ is the charge density of ions given by $n_{\text{ion},X}(\mathbf{r}, t) = \sum_{\alpha} Z_{\alpha} \delta(\mathbf{r} - \mathbf{R}_{\alpha,X}(t))$, with Z_{α} the charge number of the α th ion.

The electric current density at point X , $\mathbf{J}_X(t)$, consists of electronic and ionic contributions:

$$\mathbf{J}_X(t) = \mathbf{J}_{e,X}(t) + \mathbf{J}_{\text{ion},X}(t). \quad (50)$$

The electronic component $\mathbf{J}_{e,X}(t)$ is expressed in terms of the Bloch orbitals $u_{nk,X}(\mathbf{r}, t)$ [49], and the ionic component $\mathbf{J}_{\text{ion},X}(t)$ is given by the velocity of the ion, $(d/dt)\mathbf{R}_{\alpha,X}(t)$. Since the ionic motion induced by the pump pulse is along the x axis in the present system, the ionic current does not contribute to the one-dimensional Maxwell equation that propagates to the x direction.

We solve Eqs. (47)–(50) simultaneously to obtain the whole dynamics at once. The initial condition is so prepared that the electronic state at each macroscopic point X is set to the ground-state solution of the static density-functional theory, the ionic positions are set to their equilibrium positions in the electronic ground state, and the vector potential of the incident pump- and probe-pulsed light is prepared in the vacuum region in front of the film.

We note that the light propagation Eq. (8) can be identified with Eq. (47), if we make several assumptions and approximations. They include: we need to assume that the amplitude of the ionic motion is sufficiently small. The amplitude of the incident pulsed light needs to be sufficiently small so any nonlinear optical effects other than the Raman process can be ignorable. We also need to assume that there is no retardation effects in the electronic response that are equivalent to ignoring the frequency dependence of the susceptibilities. We will compare the first-principles calculations and the analytic formula to assess the validity of the approximations that are required to derive the analytic formula in the previous section.

B. Computational details

We carry out the simulation in the setting of the EO sampling. As the time profiles of the incident pump and probe pulses, we choose a cosine-squared-shaped envelope given as

$$\mathbf{A}_{\text{pump}}(t) = A_{\text{pump}} \cos^2\left(\frac{\pi t}{T}\right) \cos(\omega_0 t) \mathbf{e}_{011}, \quad (51)$$

$$\begin{aligned} \mathbf{A}_{\text{probe}}(t) &= A_{\text{probe}} \cos^2\left(\frac{\pi t}{T}\right) \cos(\omega_0 t) \mathbf{e}_{010} \\ &(-T/2 < t < T/2), \end{aligned} \quad (52)$$

where $\mathbf{e}_{011}(= \mathbf{e}_{yz} = (\mathbf{e}_y + \mathbf{e}_z)/\sqrt{2})$ and $\mathbf{e}_{010}(= \mathbf{e}_y)$ are the spatial unit vectors of the polarization direction of the pump and probe pulses, respectively. The incident probe pulse is given as $\mathbf{A}_{\text{probe}}(t - \delta)$ with the pump-probe delay time δ . The delay time is chosen to be 83.0, 89.5, and 96.0 fs. The average frequency ω_0 of the pump and the probe pulses are chosen to be a common value, $\hbar\omega_0 = 1.55$ eV. The pulse duration of $T = 18$ fs [from the beginning to the end of the pulse as defined in Eqs. (51) and (52)] is used for all pulses. This amounts to the pulse duration of 7 fs in FWHM. It is much shorter than the period of the optical phonon of diamond that is about 25 fs. The incident intensities of the pump and the probe pulses are set to 2×10^{12} W/cm² and 1×10^{10} W/cm², respectively. At these intensities, nonlinear electronic excitations across the band gap are not significant.

In practical calculations, we carry out calculations of the pump and the probe processes separately. In the pump stage, we calculate the propagation of the pump pulse in the medium of thickness 10 μm and the duration of 80 fs. At the final time, the pump pulse stays in the spatial region $6 \mu\text{m} < X < 10 \mu\text{m}$. In the probe stage, we prepare a diamond medium in the spatial region of $0 \mu\text{m} < X < 6 \mu\text{m}$. In this spatial region, the initial ionic motions is prepared from the coherent phonon obtained in the pump-stage calculation.

Due to the separate calculations of the pump and the probe stages, there are several effects that are ignored in the present simulation. They include effects of nonadiabatic and nonlinear electronic excitations caused by the pump pulse on the probe pulse, although it can be ignored in the present case. Also ignored are the interaction of the probe pulse with the pump pulse reflected at the surface(s) and the effect of the reflected pump pulse on the phonon. We do not include these mixed effects in the present calculations since they would make our analyses too complicated.

The calculation system and parameters are the same as those of Ref. [45]. The macroscopic coordinate X is discretized using the spacing of 15 nm. In the microscopic calculation, adiabatic local density approximation [53] is used for the exchange-correlation potential. The unit cell consisting of eight carbon atoms in the cubic cell with the side length of 3.567 Å is used. The Bloch orbitals are expressed using 16^3 uniform spatial grids in the unit cell and 12^3 of k points in the Brillouin zone. All of the equations of motion are integrated with a common time step of 0.002 fs.

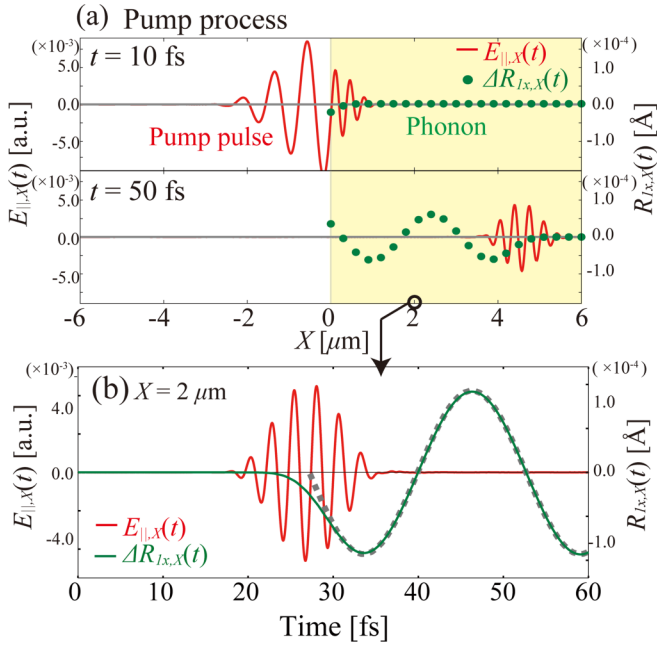


FIG. 2. Electric field and atomic displacement in the pump stage.

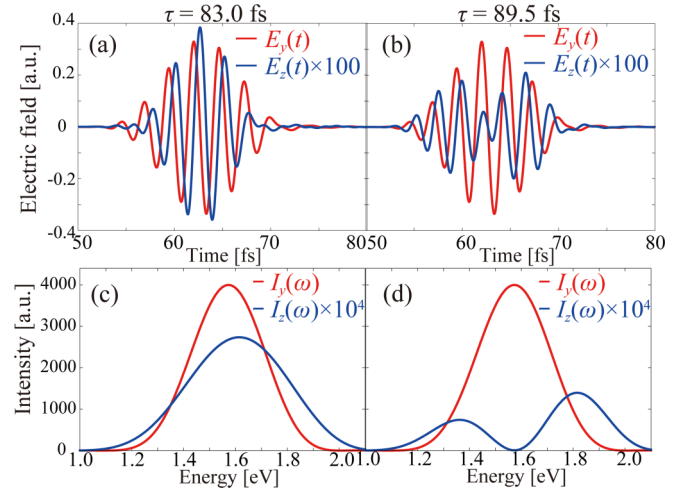
IV. CALCULATED RESULTS

The purpose of this section is to compare the results between the analytical description developed in Sec. II and the first-principles simulation described in Sec. III. Although analytical treatments provide formulas that are useful in understanding mechanisms of probe processes, several assumptions and approximations are used in the derivation including the perturbative expansion and the ignorance of the frequency dependence of the response. Contrarily, the first-principles calculation does not require these assumptions and approximations. Therefore, the comparison between two approaches will be useful to assess the validity of the analytical approach and to clarify the significance of the effects that are not included in the analytical approach.

When we make numerical evaluations of Eqs. (28), (30), (36), and (38), we use the following values for the parameters that are chosen to fit the first-principles TDDFT calculation: $n = 2.25$, $\Omega = 2\pi/(25.47[\text{fs}])$, $q_0 = 0.95 \times 10^{-4}[\text{Å}]$, and $\chi_R = 11.6[\text{Å}^{-1}]$. The values of q_0 and χ_R are so determined that the generation of the coherent phonon is described consistently by solving Eq. (8) numerically in the presence of the pump pulse.

A. Generation of coherent phonon by pump pulse

In the analytical approach, we simply assumed a sinusoidal time profile of the coherent phonon that propagates with the group velocity of the pump pulse in the medium. We first compare the time profile of the coherent phonon calculated by our multiscale simulation with the assumed one. Figure 2 shows a comparison. In panel (a), the electric field and the atomic displacement are shown two times, $t = 10$ fs when the pulse just arrived the surface and $t = 50$ fs when the pulse propagates at about $X = 4.5 \mu\text{m}$. In panel (b), the atomic displacement at $X = 2 \mu\text{m}$ is shown as a function of time. The


 FIG. 3. The transmitted electric field in y and z directions calculated by the first-principles simulation, corresponding to the transmitted probe wave and stimulated Raman wave, respectively, obtained in the right vacuum region for (a) $\delta = 83.0$ fs and (b) 89.5 fs, and their Fourier transformed power spectra for (c) $\delta = 83.0$ fs and (d) 89.5 fs.

calculated displacement shown by a solid curve is well fitted by a sinusoidal function that is shown by a dashed curve. To compare the phonon period and the pulse duration, the time profile of the incident pulse is shown by a red solid curve. The first-principles calculation describes the coherent phonon generation without any empirical parameters and including nonlinear and nonadiabatic effects, if any. The comparison indicates that the simple ISRS mechanism accurately describes the production stage of the coherent phonon in the present setting of the multiscale calculation.

B. Modulation in transmission

We move to the probe process. We first consider the modulation on the transmission. In the first-principles calculation, we analyze the transmitted wave that appears in the vacuum region right to the back surface. There may appear delayed transmitted waves that experience internal reflections inside the medium. Since we stop our calculation when the end of the first transmitted wave passes through the back surface, we do not take into account these waves of multiple reflections at the surfaces.

We first show shapes of the transmitted waves. Figures 3(a) and 3(b) show the transmitted electric field for two different pump-probe time delays, $\delta = 83.0$ fs and 89.5 fs, respectively. In the former case of $\delta = 83.0$, the probe pulse arrives at the surface of the diamond when the phonon amplitude is the maximum. In the latter case of $\delta = 89.5$ fs, the probe pulse arrives at the surface when the phonon amplitude shows the node.

In our first-principles calculation, we employ the probe pulse with the polarization in the y direction. During the propagation, the stimulated Raman wave grows linearly with the propagation length and appears as the z component of the field. In the notation of Sec. II, the z component of the electric field $E_z(x, t)$ is equal to $\sqrt{2}\delta E_{||}(x, t)$. As is shown in Eq. (16), the transmitted wave is composed of two terms, the boundary

term that is created at the surface of the medium and the bulk term that is linearly proportional to the propagation distance. The relative significance of the two terms depends on the duration of the probe pulse, phonon frequency, and propagation distance. In the present setting with the propagation distance of $6 \mu\text{m}$, the bulk contribution is much more dominant than the boundary contribution. Therefore, we expect the form

$$E_z(x, t) \propto x \frac{d}{dt} \left[q \left(t - \frac{nx}{c} \right) e^{(i)} \left(t - \frac{nx}{c} - \delta \right) \right]. \quad (53)$$

The pulse shapes in Figs. 3(a) and 3(b) indeed show the expected behavior. In the case of $\delta = 83.0$ fs, the envelope shape of the stimulated Raman wave is similar to that of the transmitted probe pulse. There is a phase shift of $\pi/2$ between the incident [$E_y(t)$] and the stimulated Raman [$E_z(t)$] waves. This is understood as follows: Since the duration of the probe pulse is shorter than the period of the phonon, the product $q(t)e^{(i)}(t)$ is mostly proportional to $e^{(i)}(t)$. The time derivative causes the phase shift of $\pi/2$. In the case of $\delta = 89.5$ fs the shape of the stimulated Raman wave is very different from the probe pulse. This is because the probe pulse propagates with the nodal point of the phonon so the product $q(t)e^{(i)}(t)$ behaves approximately as $q(t)e^{(i)}(t) \propto te^{(i)}(t)$. This explains the nodal behavior in the Raman wave at $\delta = 89.5$ fs.

In Figs. 3(c) and 3(d), frequency-resolved intensities are shown for $E_y(t)$ and $E_z(t)$. At $\delta = 83.0$ fs, the spectrum of the Raman wave shows a somewhat wider distribution and is slightly shifted to the higher frequency. At $\delta = 89.5$ fs, the spectrum of the Raman wave shows a double-peak structure. This originates from the extra node in the time domain.

In Fig. 4(a), transmission changes without frequency resolution in the first-principles calculation are shown by dots for three different pump-probe delay times, $\delta = 83.0$, 89.5 , and 96.0 fs. The delay time $\delta = 96.0$ fs corresponds to the arrival of the probe pulse at the maximum of the phonon amplitude, as in $\delta = 83.0$ fs. The modulation is large at $\delta = 89.5$ fs and very small at $\delta = 83.0$ fs and 96.0 fs. This is reasonable according to Eq. (37), since the phonon velocity is maximum at $\delta = 89.5$ fs at the nodal point. The modulation of the transmission signal calculated by the first-principles calculation coincides accurately with the analytics formula of Eq. (38) that shows a cosinelike dependence. For the plots of the analytical calculations, since we consider the transmitted wave that appears in the right vacuum region, we multiply a factor of 2 for the term of the boundary effect to take into account the transmission through two boundaries. This may be justified for the present comparison where the reflection of the pump pulse is not taken into account in the pump-stage calculation. We note that the phonon amplitude at the back surface is larger than the front surface due to the interference effect, if we consider the reflection of the pump pulse at the back surface.

We thus find a satisfactory coincidence between results of the analytic theory and those by the first-principles calculation. This fact indicates that the analysis based on the model presented in Sec. II is sufficient to describe the modulation of the transmission signal. Namely, the modulation in the present case that is dominated by the stimulated Raman wave can be accurately described using the classical model of the light propagation with harmonic oscillator approximation for the

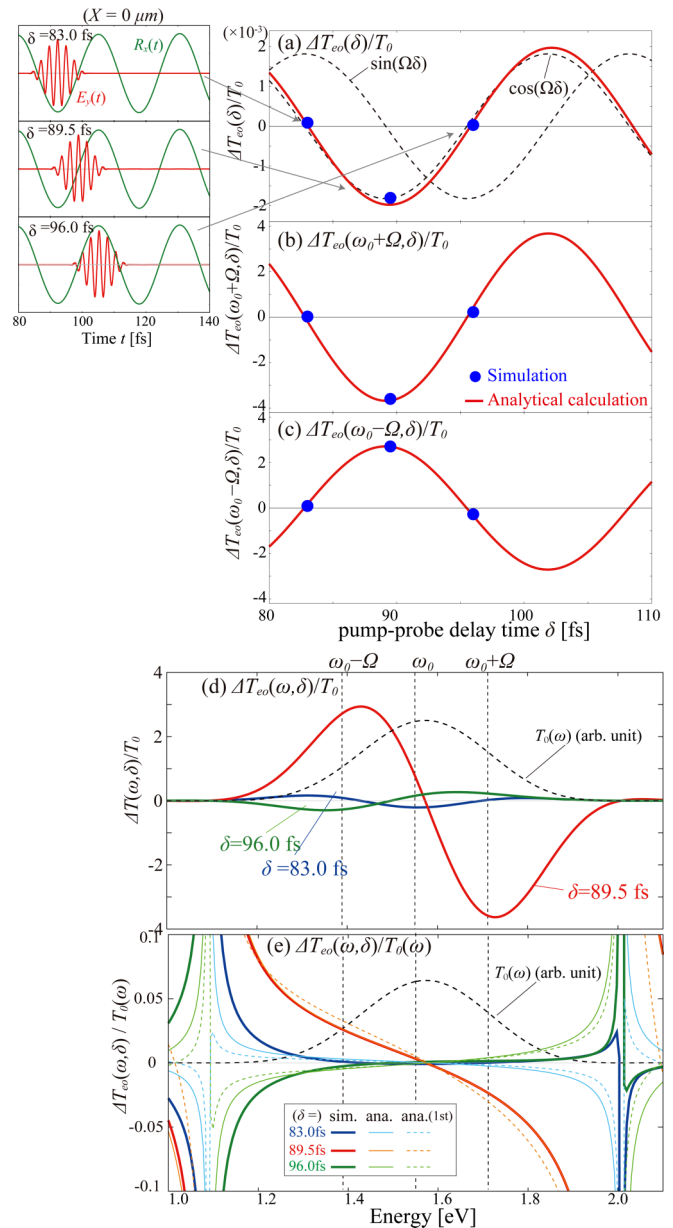


FIG. 4. (a) Transmission change $[\Delta T_{\text{EO}}(\delta)/T_0]$ and the frequency components at (b) anti-Stokes and (c) Stokes positions $[\Delta T_{\text{EO}}(\omega_0 \pm \Omega, \delta)/T_0]$, respectively] as a function of delay time δ obtained by the simulation (the blue filled circles) and the analytical calculations of Eqs. (42) and (41) [but T_0 is used instead of $T_0(\omega)$] (the red lines). The insets in (a) show the probe pulses (the red lines) and atomic displacement (the green lines) as a function of t at $X = 0 \mu\text{m}$ in the simulation for each δ . Spectrally resolved transmission change as a function of ω : (d) $\Delta T_{\text{EO}}(\omega, \delta)/T_0$, obtained by the simulation and (e) $\Delta T_{\text{EO}}(\omega, \delta)/T_0(\omega)$ by the simulations and analytical calculations [Eqs.(41) and (46)].

phonon motion, first-order expansion in the light intensity, and ignorance of dispersion effects in both the diagonal dielectric function and the off-diagonal Raman tensor. The modulation is caused mainly by the stimulated Raman wave in the present case.

In Figs. 4(b) and 4(c), modulations at the anti-Stokes and Stokes frequencies, $\omega_0 \pm \Omega$, are shown as a function of the

pump-probe delay time, δ . The first-principles and the analytical calculations show again excellent agreement. It is noted that the signal shows a striking phase difference between two components at anti-Stokes and Stokes frequencies.

To investigate the frequency-dependent modulation in detail, frequency-resolved modulation of the transmission is shown in Figs. 4(d) and 4(e) for three cases of delayed time, $\delta = 83.0, 89.5,$ and 96.0 fs at which the signals are plotted in Figs. 4(a)–4(c). As seen in Fig. 4(d), the modulation is maximum at $\delta = 89.5$ fs when the probe pulse moves with the nodal point of the coherent phonon. It also shows a phase change across approximately the central frequency of the probe pulse, 1.55 eV. The modulation is rather small at the delay times of $\delta = 83.0$ and 96.0 fs. These findings are consistent with the first term of Eq. (46) that shows the differential of the spectrum of the incident pulse.

In Fig. 4(e), the modulation divided by the frequency-resolved transmission is shown. This is the quantity often analyzed in experimental analyses. Here three lines are shown for each pump-probe delay time. Solid thick lines show the first-principles calculation, solid thin lines show analytical results using Eq. (36), and thin dashed lines show approximate analytical results using Eq. (46). The signal is again strong at $\delta = 89.5$ fs. The modulation shows a nodal structure around the average frequency of the pulse and becomes larger as the frequency apart from the average frequency. The first-principles calculation coincides accurately with the analytic formula of Eq. (36). The simplified analytic formula of Eq. (46) somewhat deviates from others. The difference is not very significant. At $\delta = 83.0$ and 96.0 fs, the signal is small for all frequencies. As the frequency comes apart from the central frequency of the probe pulse, the signal becomes larger. However, the signal showing divergent behavior at frequencies around 1.1 eV and 2.0 eV will not be physically significant since the component of the probe pulse in those frequency region is extremely small. Looking at Fig. 4(e) in detail, the signal at $\delta = 96.0$ fs shows a negative (positive) modulation at low- (high-) frequency region in both first-principles and analytic results. However, at $\delta = 83.0$ fs, though the analytic formula suggests opposite behavior while the first-principles calculation shows positive modulation on both sides. We do not have an explanation for this observation.

C. Modulation in reflection

We next consider the modulation in the reflectivity. In the first-principles calculation, the reflected wave in the vacuum region left to the surface is composed of that by the direct reflection at the front surface ($X = 0 \mu\text{m}$) and that by the reflection at the back surface ($X = 6 \mu\text{m}$) after the propagation inside the medium. The latter component includes a stimulated Raman wave while the former does not. In the first-principles calculation, the former reflected wave contains an extremely weak \hat{z} component, while the latter reflected wave accompanying a substantial \hat{z} component comes from the stimulated Raman wave. We first discuss the contribution of the former process without the propagation inside the medium.

The reflection change is shown in Fig. 5(a) by dots for three different pump-probe delay times of $\delta = 83.0,$

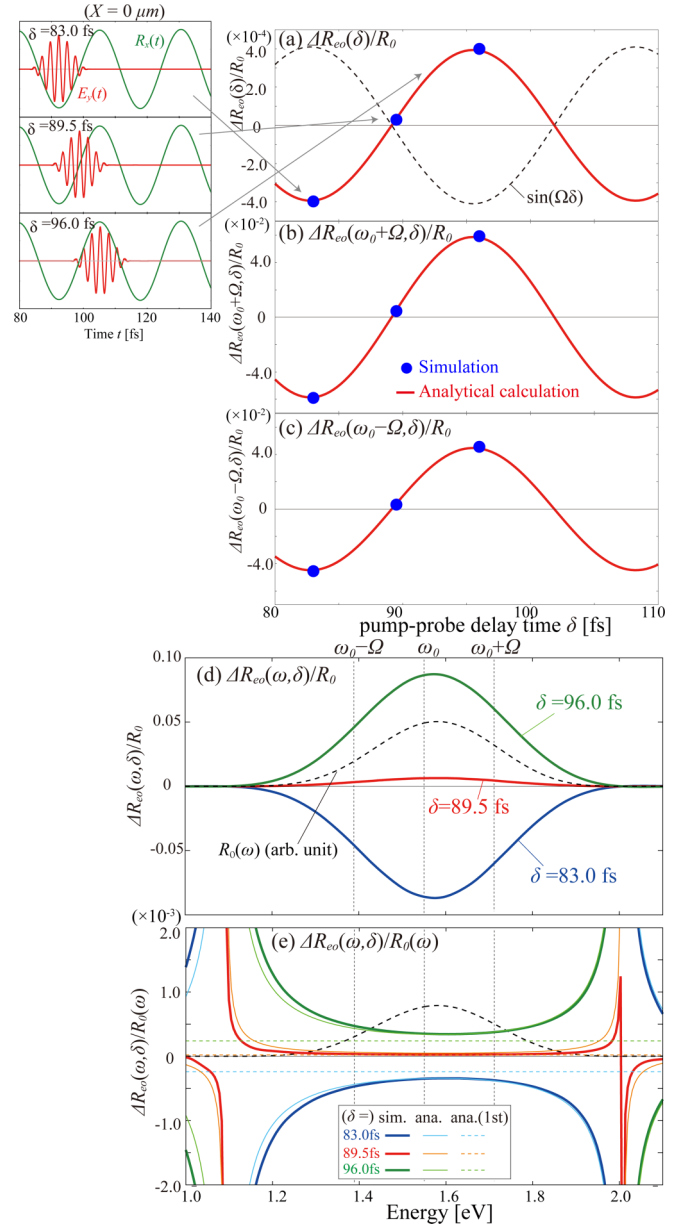


FIG. 5. (1) Reflection change $[\Delta R_{EO}(\delta)/R_0]$ and the frequency components at (b) anti-Stokes and (c) Stokes positions $[\Delta R_{EOEO}(\omega_0 \pm \Omega, \delta)/R_0]$, respectively] as a function of delay time δ obtained by the simulation (the filled blue circles) and the analytical calculations of Eqs. (32) and (33) [but R_0 is used instead of $R_0(\omega)$] (the red lines). The insets in (a) show the probe pulses (the red lines) and atomic displacement (the green lines) as a function of t at $X=0 \mu\text{m}$ in the simulation for each δ . Spectrally resolved reflection change as a function of ω : (d) $\Delta R_{EO}(\omega, \delta)/R_0$ obtained by the simulation and (e) $\Delta R_{EO}(\omega, \delta)/R_0(\omega)$ by simulations and analytical calculations [Eqs. (32) and (45)].

89.5, and 96.0 fs. The modulation in the reflection calculated by the first-principles calculation coincides accurately with the analytic formula of Eq. (30) that shows a sinelike dependence. In Figs. 5(b) and 5(c), the frequency-dependent modulation at $\omega_0 \pm \Omega$ is shown. They show a similar sinelike behavior and are again well reproduced by the analytic formula. Therefore, the validity of the analytic

formula is confirmed with high accuracy for the reflected wave.

In Figs. 5(d) and 5(e), we show modulation of the reflectivity in frequency domain. The frequency-resolved modulation divided by the reflectivity with/without frequency resolution is shown in the Figs. 5(e)/5(d), respectively. As seen in Fig. 5(d), the modulation has a similar frequency dependence with the frequency-resolved flux of the incident wave. The frequency-resolved reflectivity shown in Fig. 5(e) indicates that the frequency dependence of the modulation is rather weak. In the frequency region far apart from the central frequency, the modulation becomes larger. However, the incident flux does not have much of a component in such a frequency region. We find good agreement among three curves, the first-principles calculation, the analytic formula of Eq. (32), and the simplified analytic formula of Eq. (45). The agreement indicates that the analytic formulas are sufficiently accurate to describe the modulation in the reflectivity.

D. Reflection at the back surface

We next examine the modulation in the reflection, including the reflected wave caused by the back surface. In Fig. 6(a), we show a time profile of the reflection waves reflected from the front surface and from the back surface of the medium in the first-principles calculation. The z component of the field is very small in the first wave from the front surface, while that of the second wave from the back side is much larger because of the amplification of the Raman wave during the propagation. The reflection change $\Delta R_{EO}(\delta)/R_0$ is shown in Fig. 6(b) for three pump-probe delay times, $\delta = 83.0$, 89.5 , and 96.0 fs. It can be well fit by a cosinelike function. This can be understood as follows: In the case of the transmission, the bulk effect caused by the stimulated Raman wave is dominated as seen in Fig. 4(a). In the present case, the second reflected wave includes a similar Raman wave component as seen in the Fig. 6(a). The modulation in the reflection is dominated by the bulk effect, if we include the second reflected wave at the back surface.

Figure 6(c) shows the spectrally resolved signals calculated by using the first and second reflection waves. A strong oscillation structure is observed in the frequency domain for three cases of the time delay. The oscillation structure is due to the interference between the first and second waves: The Fourier transformed electric field of the reflection wave can be given as $\tilde{E}_1(\omega) + \tilde{E}_2(\omega)e^{i\omega(t_2-t_1)}$, where \tilde{E}_1 and \tilde{E}_2 are of the first and the second reflection waves, respectively, and t_1 and t_2 is the arrival time of the first and second waves, respectively. The power spectrum is written as $I(\omega) = |\tilde{E}_1(\omega)|^2 + |\tilde{E}_2(\omega)|^2 + 2\text{Re}[\tilde{E}_1^*(\omega)\tilde{E}_2(\omega)e^{i\omega(t_2-t_1)}]$. It indicates that the oscillation frequency is inversely proportional to the difference of the two reflected waves, $t_2 - t_1$, which is proportional to the thickness of the sample. The present calculation assumes a sample of $6\text{-}\mu\text{m}$ thickness. The oscillation will not be observed if a much thicker sample is utilized.

If we average the signals of Fig. 6(c) over rapidly oscillating structures, we obtain a very small signal for $\delta = 83.0$ and 96.0 fs, and a strong signal remains for $\delta = 89.5$ fs. The averaged feature is very close to the transmission shown in Fig. 4(d). Namely, the signal is caused mainly by the Raman

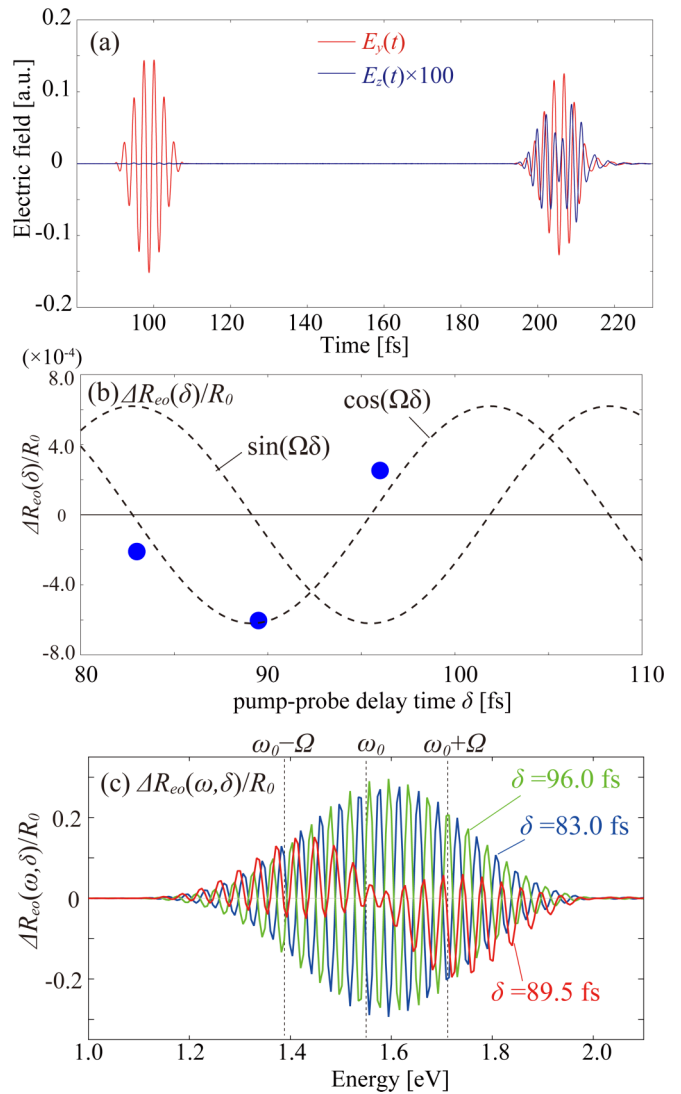


FIG. 6. (a) Example of the reflection wave from the front surface and the back side detected at the left vacuum region ($\delta = 89.5$ fs). (b) Reflection change as a function of δ taking into account the reflection waves from both surfaces and (c) their spectrally resolved reflection changes.

wave that is included in the second wave of Fig. 6(a) and that is quite similar to that in the transmitted wave.

V. SUMMARY

We have presented a comprehensive theoretical analysis on the probe stage of pump-probe measurements of coherent phonon generation in dielectrics. We take a diamond as a typical case and assume the ISRS mechanism for the generation process.

We have developed analytical and computational approaches. In analytical description, we revisited the work developed in Ref. [5] by Merlin and developed a comprehensive formula. We start with a standard description of light propagation coupled with a phonon motion through the Raman tensor. We summarize the formula for the modulation on the reflection and transmission of the probe pulse using

a perturbative solution for the probe pulse. The modulation in the transmission is caused by two distinct mechanisms: the boundary and the bulk effects. The bulk effect is caused by the stimulated Raman wave that is amplified as the probe pulse propagates in the medium. The modulation in the reflection is caused by the boundary effect. However, if we consider the reflection at the back surface, the bulk effect also contributes in the reflection.

The modulation is investigated for frequency-resolved and -integrated signals. The boundary and the bulk effects contribute to the modulation in a qualitatively different way. The bulk effect produces strong frequency dependence in the modulation, whereas the boundary effect produces very weak frequency dependence. The bulk effect causes strong modulation in the probe signal when the probe pulse moves with the nodal point of the phonon. It causes a phase shift of $\pi/2$ between the phonon amplitude and the probe signal. Contrarily, the boundary effect causes a modulation that is proportional to the amplitude of the phonon. The modulation of the probe pulse is in phase with the coherent phonon.

The derivation of the analytic formula is based on several assumptions and approximations. To confirm the validity of the analytic formula, we performed first-principles calculations based on TDDFT. In our multiscale formalism, coupled dynamics of mesoscopic light propagation and microscopic electronic and ionic motions are described simultaneously without any empirical parameters.

By comparing results between the analytical theory and the first-principles calculation, we confirmed the validity and the reliability of the analytical formula. We thus consider that our analytic formula provides a reliable basis for the experimental analysis of frequency-resolved modulation in the pump-probe measurement of coherent phonon in transparent dielectrics.

However, we should note that the relative significance of the surface and the bulk effects in actual experimental conditions is a delicate issue [5,38], as we noted in the Introduction. Since the bulk effect is proportional to the optical path length while the surface effect is not, an analysis changing the film thickness would be useful to clarify their relative significance. Interference effects may also introduce interesting physics in thin films. We plan to explore it in our next publication.

ACKNOWLEDGMENTS

We thank Professor K. G. Nakamura for useful discussion. We acknowledge the support by JST-CREST under Grant No. JP-MJCR16N5 and by MEXT as a priority issue theme No. 7 to be tackled by using Post-K Computer, and by JSPS KAKENHI Grant No. 15H03674. Calculations are carried out at Oakforest-PACS at JCAHPC through the Multidisciplinary Cooperative Research Program in CCS, University of Tsukuba, and through the HPCI System Research Project (Project No. hp180088).

-
- [1] C. Thomsen, J. Strait, Z. Vardeny, H. J. Maris, J. Tauc, and J. J. Hauser, Coherent Phonon Generation and Detection by Picosecond Light Pulses, *Phys. Rev. Lett.* **53**, 989 (1984).
- [2] Y.-X. Yan, E. B. Gamble, Jr., and K. A. Nelson, Impulsive stimulated scattering: General importance in femtosecond laser pulse interactions with matter, and spectroscopic applications, *J. Chem. Phys.* **83**, 5391 (1985).
- [3] Y. X. Yan and K. A. Nelson, Impulsive stimulated light scattering. I. General theory, *J. Chem. Phys.* **87**, 6240 (1987).
- [4] G. C. Cho, W. Kütt, and H. Kurz, Subpicosecond Time-Resolved Coherent-Phonon Oscillations in GaAs, *Phys. Rev. Lett.* **65**, 764 (1990).
- [5] R. Merlin, Generating coherent THz phonons with light pulses, *Solid State Commun.* **102**, 207 (1997), Highlights in Condensed Matter Physics and Materials Science.
- [6] T. E. Stevens, J. Kuhl, and R. Merlin, Coherent phonon generation and the two stimulated Raman tensors, *Phys. Rev. B* **65**, 144304 (2002).
- [7] M. Hase, M. Kitajima, A. M. Constantinescu, and H. Petek, The birth of a quasiparticle in silicon observed in time-frequency space, *Nature* **426**, 51 (2003).
- [8] K. Ishioka, M. Hase, M. Kitajima, and H. Petek, Coherent optical phonons in diamond, *App. Phys. Lett.* **89**, 231916 (2006).
- [9] K. Mizoguchi, R. Morishita, and G. Oohata, Generation of Coherent Phonons in a CdTe Single Crystal Using an Ultrafast Two-Phonon Laser-Excitation Process, *Phys. Rev. Lett.* **110**, 077402 (2013).
- [10] K. G. Nakamura, K. Ohya, H. Takahashi, T. Tsuruta, H. Sasaki, S. Uozumi, K. Norimatsu, M. Kitajima, Y. Shikano, and Y. Kayanuma, Spectrally resolved detection in transient-reflectivity measurements of coherent optical phonons in diamond, *Phys. Rev. B* **94**, 024303 (2016).
- [11] H. Sasaki, R. Tanaka, Y. Okano, F. Minami, Y. Kayanuma, Y. Shikano, and K. G. Nakamura, Coherent control theory and experiment of optical phonons in diamond, *Sci. Rep.* **8**, 9609 (2018).
- [12] S. De Silvestri, J. G. Fujimoto, E. P. Ippen, Edward B. Gamble, Jr., Leah Ruby Williams, and Keith A. Nelson, Femtosecond time-resolved measurements of optic phonon dephasing by impulsive stimulated Raman scattering in α -perylene crystal from 20 to 300 K, *Chem. Phys. Lett.* **116**, 146 (1985).
- [13] L. Dhar, J. A. Rogers, and K. A. Nelson, Time-resolved vibrational spectroscopy in the impulsive limit, *Chem. Rev.* **94**, 157 (1994).
- [14] T. K. Cheng, J. Vidal, H. J. Zeiger, G. Dresselhaus, M. S. Dresselhaus, and E. P. Ippen, Mechanism for displacive excitation of coherent phonons in Sb, Bi, Te, and Ti_2O_3 , *Appl. Phys. Lett.* **59**, 1923 (1991).
- [15] K. Kato, A. Ishizawa, K. Oguri, K. Tateno, T. Tawara, H. Gotoh, M. Kitajima, and H. Nakano, Anisotropy in ultrafast carrier and phonon dynamics in p -type heavily doped Si, *Jpn. J. Appl. Phys.* **48**, 100205 (2009).
- [16] O. V. Misochko, Muneaki Hase, and M. Kitajima, Spectrally filtered time domain study of coherent phonons in semimetals, *J. Phys.: Condens. Matter* **16**, 1879 (2004).
- [17] M. Hase and M. Kitajima, Interaction of coherent phonons with defects and elementary excitations, *J. Phys.: Condens. Matter* **22**, 073201 (2010).
- [18] G. D. Sanders, A. R. T. Nugraha, K. Sato, J.-H. Kim, J. Kono, R. Saito, and C. J. Stanton, Theory of coherent phonons in carbon

- nanotubes and graphene nanoribbons, *J. Phys.: Condens. Matter* **25**, 144201 (2013).
- [19] T. Pfeifer, W. Kütt, H. Kurz, and R. Scholz, Generation and Detection of Coherent Optical Phonons in Germanium, *Phys. Rev. Lett.* **69**, 3248 (1992).
- [20] R. Scholz, T. Pfeifer, and H. Kurz, Density-matrix theory of coherent phonon oscillations in germanium, *Phys. Rev. B* **47**, 16229 (1993).
- [21] A. V. Kuznetsov and C. J. Stanton, Theory of Coherent Phonon Oscillations in Semiconductors, *Phys. Rev. Lett.* **73**, 3243 (1994).
- [22] D. M. Riffe and A. J. Sabbah, Coherent excitation of the optic phonon in Si: Transiently stimulated Raman scattering with a finite-lifetime electronic excitation, *Phys. Rev. B* **76**, 085207 (2007).
- [23] F. Glerean, S. Marcantoni, G. Sparapassi, A. Blason, M. Esposito, F. Benatti, and D. Fausti, Quantum model for impulsive stimulated Raman scattering, *J. Phys. B: At. Mol. Opt. Phys.* **52**, 145502 (2019).
- [24] Y. Watanabe, K. Hino, N. Maeshima, H. Petek, and M. Hase, Ultrafast asymmetric Rosen-Zener-like coherent phonon responses observed in silicon, *Phys. Rev. B* **99**, 174304 (2019).
- [25] Y.-H. Cheng, F. Y. Gao, S. W. Teitelbaum, and K. A. Nelson, Coherent control of optical phonons in bismuth, *Phys. Rev. B* **96**, 134302 (2017).
- [26] S. Wall, D. Wegkamp, L. Foglia, K. Appavoo, J. Nag, R. F. Haglund, Jr., J. Stähler, and M. Wolf, Ultrafast changes in lattice symmetry probed by coherent phonons, *Nat. Commun.* **3**, 721 (2012).
- [27] K. Iwano, Y. Shimoi, T. Miyamoto, D. Hata, M. Sotome, N. Kida, S. Horiuchi, and H. Okamoto, Ultrafast Photoinduced Electric-Polarization Switching in a Hydrogen-Bonded Ferroelectric Crystal, *Phys. Rev. Lett.* **118**, 107404 (2017).
- [28] S. Horiuchi, K. Kobayashi, R. Kumai, and S. Ishibashi, Proton tautomerism for strong polarization switching, *Nat. Commun.* **8**, 14426 (2017).
- [29] T. Frigge, B. Hafke, T. Witte, B. Krenzer, C. Streubühr, A. Samad Syed, V. Mikšić Trontl, I. Avigo, P. Zhou, M. Ligges, D. von der Linde, U. Bovensiepen, M. Horn von Hoegen, S. Wippermann, A. Lücke, S. Sanna, U. Gerstmann, and W. G. Schmidt, Optically excited structural transition in atomic wires on surfaces at the quantum limit, *Nature* **544**, 207 (2017).
- [30] M. F. Jagera, C. Otta, P. M. Krausa, C. J. Kaplana, W. Pousea, R. E. Marvelc, R. F. Haglundc, D. M. Neumarka, and S. R. Leone, Tracking the insulator-to-metal phase transition in VO₂ with few-femtosecond extreme UV transient absorption spectroscopy, *Proc. Natl. Acad. Sci. USA* **114**, 9558 (2017).
- [31] D. M. Fritz, D. A. Reis, B. Adams, R. A. Akre, J. Arthur, C. Blome, P. H. Bucksbaum, A. L. Cavalieri, S. Engemann, S. Fahy, R. W. Falcone, P. H. Fuoss, K. J. Gaffney, M. J. George, J. Hajdu, M. P. Hertlein, P. B. Hillyard, M. Horn von Hoegen, M. Kammler, J. Kaspar, R. Kienberger, P. Krejčík, S. H. Lee, A. M. Lindenberg, B. McFarland, D. Meyer, T. Montague, E. D. Murray, A. J. Nelson, M. Nicoul, R. Pahl, J. Rudati, H. Schlarb, D. P. Siddons, K. Sokolowski-Tinten, Th. Tschentscher, D. von der Linde, and J. B. Hastings, Ultrafast bond softening in bismuth: Mapping a solid's interatomic potential with x-rays, *Science* **315**, 633 (2007).
- [32] K. Sokolowski-Tinten, C. Blome, J. Blums, A. Cavalleri, C. Dietrich, A. Tarasevitch, I. Uschmann, E.-Förster, M. Kammler, M. H. von Hoegen, and D. von der Linde, Femtosecond X-ray measurement of coherent lattice vibrations near the Lindemann stability limit, *Nature* **422**, 287 (2003).
- [33] B. Bauerhenne, E. S. Zijlstra, and M. E. Garcia, Molecular dynamics simulations of a femtosecond-laser-induced solid-to-solid transition in antimony, *Appl. Phys. A* **123**, 608 (2017).
- [34] K. Ishioka, M. Hase, and M. Kitajima, Ultrafast electron-phonon decoupling in graphene, *Phys. Rev. B* **77**, 121402 (2008).
- [35] I. Katayama, K. Sato, S. Koga, J. Takeda, S. Hishita, H. Fukidome, M. Suemitsu, and M. Kitajima, Coherent nanoscale optical-phonon wave packet in graphene layers, *Phys. Rev. B* **88**, 245406 (2013).
- [36] K. Sato, K. Tahara, Y. Minami, I. Katayama, M. Kitajima, H. Kawai, K. Yanagi, and J. Takeda, Resonance enhancement of first- and second-order coherent phonons in metallic single-walled carbon nanotubes, *Phys. Rev. B* **90**, 235435 (2014).
- [37] T. Nakayama, S. Yoshizawa, A. Hirano, T. Tanaka, K. Shiraki, and M. Hase, Vibrational energy transfer from photoexcited carbon nanotubes to proteins observed by coherent phonon spectroscopy, *App. Phys. Exp.* **10**, 125101 (2017).
- [38] Y. Liu, A. Frenkel, G. A. Garrett, J. F. Whitaker, S. Fahy, C. Uher, and R. Merlin, Impulsive Light Scattering by Coherent Phonons in LaAlO₃: Disorder and Boundary Effects, *Phys. Rev. Lett.* **75**, 334 (1995).
- [39] E. Runge and E. K. U. Gross, Density-Functional Theory for Time-Dependent Systems, *Phys. Rev. Lett.* **52**, 997 (1984).
- [40] C. A. Ullrich, *Time-Dependent Density-Functional Theory: Concepts and Applications*, Oxford Graduate Texts (Oxford University Press, Oxford, United Kingdom, 2012).
- [41] K. Yabana and G. F. Bertsch, Time-dependent local-density approximation in real time, *Phys. Rev. B* **54**, 4484 (1996).
- [42] G. F. Bertsch, J.-I. Iwata, A. Rubio, and K. Yabana, Real-space, real-time method for the dielectric function, *Phys. Rev. B* **62**, 7998 (2000).
- [43] Y. Shinohara, K. Yabana, Y. Kawashita, J.-I. Iwata, T. Otobe, and G. F. Bertsch, Coherent phonon generation in time-dependent density functional theory, *Phys. Rev. B* **82**, 155110 (2010).
- [44] Y. Shinohara, S. A. Sato, K. Yabana, J.-I. Iwata, T. Otobe, and G. F. Bertsch, Nonadiabatic generation of coherent phonons, *J. Chem. Phys.* **137**, 22A527 (2012).
- [45] A. Yamada and K. Yabana, Multiscale time-dependent density functional theory for a unified description of ultrafast dynamics: Pulsed light, electron, and lattice motions in crystalline solids, *Phys. Rev. B* **99**, 245103 (2019).
- [46] A. Yamada, Multiscale coupled Maxwell's equations and polarizable molecular dynamics simulation based on charge response kernel model, *J. Chem. Phys.* **152**, 094110 (2020).
- [47] S. Yamada, M. Noda, K. Nobusada, and K. Yabana, Time-dependent density functional theory for interaction of ultrashort light pulse with thin materials, *Phys. Rev. B* **98**, 245147 (2018).
- [48] R. Jestädt, M. Ruggenthaler, M. J. T. Oliveira, A. Rubio, and H. Appel, Light-matter interactions within the Ehrenfest–Maxwell–Pauli–Kohn–Sham framework: Fundamentals, implementation, and nano-optical applications, *Adv. Phys.* **68**, 225 (2019).

- [49] K. Yabana, T. Sugiyama, Y. Shinohara, T. Otobe, and G. F. Bertsch, Time-dependent density functional theory for strong electromagnetic fields in crystalline solids, *Phys. Rev. B* **85**, 045134 (2012).
- [50] M. Noda, S. A. Sato, Y. Hirokawa, M. Uemoto, T. Takeuchi, S. Yamada, A. Yamada, Y. Shinohara, M. Yamaguchi, K. Iida, I. Floss, T. Otobe, K.-M. Lee, K. Ishimura, T. Boku, G. F. Bertsch, K. Nobusada, and K. Yabana, SALMON: Scalable *ab-initio* light-matter simulator for optics and nanoscience, *Comput. Phys. Commun.* **235**, 356 (2019).
- [51] Web site of SALMON, <http://salmon-tddft.jp/>.
- [52] N. Troullier and J. L. Martins, Efficient pseudopotentials for plane-wave calculations, *Phys. Rev. B* **43**, 1993 (1991).
- [53] J. P. Perdew and Alex Zunger, Self-interaction correction to density-functional approximations for many-electron systems, *Phys. Rev. B* **23**, 5048 (1981).